Deformation Velocity-Based Regularization of Multibaseline SAR Interferometry

Roghayeh Zamani and Hossein Aghababaei, *Senior Member, IEEE*

***Abstract*— Synthetic aperture radar (SAR) interferometry (InSAR) has shown great potential in the monitoring of Earth's surface and detection of the possible slow temporal deformations. Within the framework of multibaseline SAR interferometry, the availability of multiple interferograms obtained from multipass satellite observations can significantly improve the accuracy of the estimated target parameters, i.e., the residual height and the mean deformation velocity. The parameters can be estimated in the maximum likelihood (ML) sense and through the data covariance matrix. However, the presence of artifact and outliers may impair the parameter estimation, specifically when the candidate cells are subject to temporal decorrelation and atmospheric phase noise effects. In this letter, the exploitation of contextual spatial information is proposed to reduce the possible ambiguity and improve the accuracy of ML-based parameter estimation. The proposed approach adds a regularization term (or a constraint) to the ML's model in order to include the information about the scene velocity variation. Hence, the resulted nonconvex optimization is resolved using the graph-cut concept. The method is evaluated using the simulated and two real data sets acquired by Constellation of Small Satellites for Mediterranean basin Observation (COSMO-SkyMed) and Sentinel-1A sensors over Tehran, Iran; and the results are validated using the global positioning system-based measurements.**

***Index Terms*— Multibaseline (MB) SAR interferometry, regularization term, synthetic aperture radar (SAR).**

I. Introduction

THE differential synthetic aperture radar (SAR) interferometry is today well assessed and broadly exploited in remote sensing of complex environments in order to measure Earth's surface displacements [1]. The technique aims to identify stable scatterers and exploit their interferometric phase to measure the ground displacement. In the literature, the main experimented and investigated multibaseline (MB) techniques to improve the density of the network of scatterers, which is the necessity for accurate modeling of earth surface displacement, rely on multilook framework [2]. These techniques, such as SqueeSAR [1], commonly exploit spatial multilooking to estimate the data covariance matrix, which is subsequently used to characterize additionally extended (and weaker) targets, termed as distributed scatterers. Other multilook techniques in maximum likelihood (ML) sense [3], [4] take the benefits of both amplitude and phase of interferometric data and take into account the mutual correlation of all the acquired images to estimate the geophysical parameters (i.e., the residual height and mean deformation velocity).

Typically, these techniques require the scatterer to possess some fundamental specifications: the target's reflectivity is constant over all acquisitions and its interferometric phase is related to the nominal distance between sensor and target. In reality, however, temporal decorrelation and unmodeled phase error (e.g., from nonoptimal atmospheric compensation) can significantly compromise the performance of these techniques.

In [5], the robust M-estimator in multipass interferometry was introduced to optimally treat the data with phase error. However, in this letter, in order to enhance the capability of the ML-based approach, when dealing with both the above-mentioned limitations, a *regularization* procedure is proposed. The technique adapts a regularization term of velocity variation over the spatial neighborhood pixels to the ML's model. The added term allows trading-off the solution of ML and the velocity variation within the neighborhood pixels, leading to the mitigation of possible interferometric artifacts and noise perturbations. The interaction between ML and regularized term defines a nonconvex optimization problem that is resolved using the concept of graph-cut minimization-based strategy [6].

This letter is organized as follows. Section II describes the methodology, including a brief review of ML estimation and an explanation of the proposed framework. In Section III, the experimental results from the simulated and real data sets are shown by pointing out the improvements obtained by the proposed method. Finally, the conclusions and discussion are presented in Section IV.

II. Methodology

A. SAR Data Model

Let us refer to a stack of N complex single-look (SLC) SAR data of the same area obtained in multitemporal MB configuration using a sensor that operates at wavelength λ and range distance ρ. The images are obtained along different trajectories distinct by orthogonal spatial and temporal baselines b_n and t_n from a reference master acquisition. Assume that the stack data are coregistered with respect to a given master image, and therefore, the resulting complex target vector $\mathbf{x}$ for a specific pixel p can be represented by

$$\mathbf{x}(p) = [x_1(p) \quad x_1(p) \quad \ldots\ldots \quad x_N(p)]^{\mathrm{T}} \tag{1}$$

where $x_k(p)$ is the complex measurement of pixel p in the kth image and T indicates the transpose operator. The measured MB target vector $\mathbf{x}(p)$ has circular Gaussian random distribution with the zero mean and its covariance matrix is given by $\mathbf{R} = E[\mathbf{x}(p)\mathbf{x}(p)^{\dagger}]$, where $E[.]$ and $\dagger$are the expectation and Hermitian operators, respectively.

Manuscript received July 7, 2020; revised September 1, 2020; accepted September 29, 2020. Date of publication October 12, 2020; date of current version December 21, 2021. *(Corresponding author: Roghayeh Zamani.)*

Roghayeh Zamani is with the Faculty of Geomatics Engineering, K.N. Toosi University of Technology, Tehran 1969764499, Iran (e-mail: zamani@mail.kntu.ac.ir).

Hossein Aghababaei is with the Faculty of Geo-Information Science and Earth Observation (ITC), University of Twente, 7522 Enschede, The Netherlands.

Digital Object Identifier 10.1109/LGRS.2020.3028244

It should be noted that MB data sets are assumed to be compensated for the flat-earth effect (*f.i.* using the orbital information) and topographic phase effect [i.e., using low-resolution external terrain model, e.g., Shuttle Radar Topography Mission (SRTM)].

Additionally, we implicitly assumed that atmospheric phase is spatially constant over the image, and the data were calibrated with respect to one pixel whose deformation is known (typically a high coherent pixel located in a nondeforming zone, which is characterized by *a priori* information about the test site). Note that the assumption is valid and the calibration is acceptable for a small/local area, such as the considered test sites in this study.

B. Nonlocal Estimation of Data Covariance Matrix

The covariance matrix estimation is one of the important processing steps of multilook interferometry. Generally, the true covariance matrix is unknown and it is commonly approximated using the sample covariance matrix (SCM). In the InSAR literature, SCM is typically computed based on the statistical distribution test [1]. However, in this study, a nonlocal (NL) technique based on the generalized likelihood ratio (GLR) test is employed. The technique is called NLSAR [7], and it estimates SCM by weighted averaging over all pixels (q) in a search window that is centralized around the pixel of interest (p), that is,

$$\hat{\mathbf{R}}^{\mathrm{NL}}(p) = \sum_{q} w(p,q)\mathbf{x}(q)\mathbf{x}(q)^{\dagger} \Big/ \sum_{q} w(p,q) \tag{2}$$

where $\hat{\mathbf{R}}^{\mathrm{NL}}$ indicates the NL-based SCM of pixel p, while w represents the sample's relative importance. For more details on the implementation of NLSAR, the readers are referred to [7].

C. ML Interferometric Framework

The key feature of the ML-based approach is related to the assumption that the complex target vector $\mathbf{x}$ in (1) is distributed according to the Goodman's model and follows a zero-mean circular complex Gaussian distribution as [8]:

$$f(\mathbf{x}|\mathbf{R}) = \exp\left(-\mathbf{x}^{\dagger}\mathbf{R}^{-1}\mathbf{x}\right)/\pi\,|\mathbf{R}| \tag{3}$$

where f represents the probability density function (pdf) of vector $\mathbf{x}$. Note that in (3), the dependence of $\mathbf{x}$ and $\mathbf{R}$ on the pixel coordinate p has not explicitly indicated for the sake of notation simplicity. Let us decompose the covariance matrix as

$$\mathbf{R} = \mathbf{\Gamma}^{1/2}\,\mathbf{C}\,\mathbf{\Gamma}^{1/2} \tag{4}$$

where $\mathbf{\Gamma}$ is a diagonal matrix constructed by the diagonal elements of $\mathbf{R}$, in which $\mathbf{\Gamma}(k,k)$ represents the intensity of the kth channel, and $\mathbf{C}$ is the true coherence matrix where its elements can be represented as

$$\mathbf{C}(k,l) = \frac{E\left[x_k x_l^{\dagger}\right]}{\sqrt{E\left[x_k x_k^{\dagger}\right]E\left[x_l x_l^{\dagger}\right]}} = \gamma_{kl}\ \exp(\varphi_{kl}). \tag{5}$$

In (5), γ_{kl} and φ_{kl} are the real-valued reflectivity and interferometric phase between channels k and l, respectively. Additionally, the interferometric phase can be written as

$$\varphi_{kl} = \frac{4\pi\,(b_l - b_k)}{\lambda\rho\,\sin(\theta)}z + \frac{4\pi\,(t_l - t_k)}{\lambda}\upsilon \tag{6}$$

where θ indicates the incident angle, and the parameters z and υ represent the residual height and mean deformation velocity, respectively.

Eventually, from the pdf of the observation vector in (3), it readily can be shown that for each pixel p, the ML estimates of the unknown parameters (z, υ) are the corresponding values that minimize the following cost function [3]:

$$(\hat{z}, \hat{\upsilon}) = \arg\min_{z,\upsilon}\left(\mathrm{Trace}\left(\mathbf{C}^{-1}\hat{\mathbf{C}}^{\mathrm{NL}}\right)\right) \tag{7}$$

where Trace(.) is the trace operator and $\hat{\mathbf{C}}^{\mathbf{NL}}$ is the sample coherence matrix obtained from decomposition (4) of NL SCM $\hat{\mathbf{R}}^{\mathbf{NL}}$. From (5), the true coherence matrix $\mathbf{C}$ is the function of z, υ, and γ_{kl}, while it has to be understood that the optimization in (7) is obtained under the assumption that the reflectivity γ_{kl} is fixed to its counterpart estimation from the NL approach, i.e., $\gamma_{kl} = \hat{\gamma_{kl}}^{\mathrm{NL}}$ where $\hat{\gamma_{kl}}^{\mathrm{NL}}$ is a real value coherence between channels k and l obtained from the NL coherence matrix $\hat{\mathbf{C}}^{\mathrm{NL}}$.

Finally, the minimization problem in (7) can be resolved using numerical optimization through the joint estimation of $\hat{z}$ and $\hat{\upsilon}$. Particularly, for a pixel p, whose $\hat{\mathbf{R}}^{\mathbf{NL}}$ and consequently $\hat{\mathbf{C}}^{\mathbf{NL}}$ are estimated using the NLSAR approach, the residual height and velocity are estimated within the specified elevation $[z_{\min}\ z_{\max}]$ and velocity $[\upsilon_{\min}\ \upsilon_{\max}]$ search space. For each height and velocity level (z_l, υ_l) in the search space, the matrix $\mathbf{C}$ can be generated using (5), where its reflectivity is set to the corresponding NL estimation, i.e., $\gamma_{kl} = \hat{\gamma_{kl}}^{\mathrm{NL}}$ or $|\mathbf{C}| = |\hat{\mathbf{C}}^{\mathbf{NL}}|$. Apparently, the height and velocity that lead to the minimization of Trace$(\mathbf{C}^{-1}\hat{\mathbf{C}}^{\mathbf{NL}})$ are selected as the solution of (7). To properly define the elevation and velocity search space, the readers are referred to [9].

The ML approach is an optimal multilook framework for interferometric analysis. However, the presence of artifacts and perturbations of interferometric noise may impair the parameter estimation. To cope with this possible issue and increase the reliability of estimated parameters, the regularization of the ML approach is proposed in Section II-D.

D. Proposed Regularization Approach

The spatial characteristics or context is an important source of information. Following the idea presented in [4] and [10], we proposed to regularize the typical ML optimization model with deformation velocity variation in the neighborhood pixels. Let us consider a window centralized around a pixel p in the image. The window contains $M-1$ neighborhood samples (q) of the pixel p. The proposed framework is based on the assumption that the mean deformation velocity smoothly changes from pixel to pixel over the neighborhood samples. Hence, a constraint or *a priori* that controls the velocity variation between neighborhood samples is given by

$$\sum_{p,q} |\upsilon(q) - \upsilon(p)| \tag{8}$$

where $\upsilon(q)$ and $\upsilon(p)$ are the mean deformation velocities of neighborhood and central pixels, respectively. Hence, to control the total variation in velocity over the neighborhood samples in the considered window, the regularized ML can be denoted as

$$(\hat{\mathbf{z}}, \hat{\mathbf{v}}) = \arg\min_{\mathbf{z},\mathbf{v}} \sum_{p,q}\left[\mathrm{Trace}\left(\mathbf{C}^{-1}\hat{\mathbf{C}}^{\mathrm{NL}}\right)_{p,q} + \alpha|\upsilon(q) - \upsilon(p)|\right]. \tag{9}$$

Equation (9) is an optimization problem with respect to the height and velocity of all M pixels in the considered window. Differently from the standard ML in (7), optimization in (9)

Implementation Algorithm of the Proposed Regularized ML Approach

1. Estimate the sample covariance matrix for all pixels of the images using the NLSAR approach.
2. For each central pixel p
3. Consider its local neighborhoods within a specified window
4. For each z_l and v_l in the ranges of $[z_{min}\ z_{max}]$ and $[v_{min}\ v_{max}]$
5. Compute the data term using $Trace(\mathbf{C}^{-1}\hat{\mathbf{C}}^{\mathrm{NL}})$ for all pixels in the window and add the related nodes to the graph at levels z_l and v_l.
6. End
7. Perform minimization in (9) and derive the parameters of interest $(\hat{\mathbf{z}}, \hat{\mathbf{v}})$ for central pixel p.
8. End

has to be solved for several pixels at once. Note that $\hat{\mathbf{z}}$ and $\hat{\mathbf{v}}$ are two vectors collecting the estimated residual heights and velocities of all pixels (p and q) in the window. To solve this optimization, the graph-cut minimization-based strategy [6] is adapted. To simplify the explanation of the graph cut's concepts, Fig. 1 as a simple example of the constructed graph is shown. We assume that the search space of elevation and deformation velocity is discretized into L layers, such that each layer is a particular combination of possible elevation and the velocity (z_l, v_l) in the search space. Hence, a graph can be constructed (see Fig. 1), where each node is linked to a specific sample (horizontal axis) at a particular height z_l and velocity v_l layer (vertical axis). In particular, the nodes of the graph are related to the data terms Trace$(\mathbf{C}^{-1}\hat{\mathbf{C}}^{\mathbf{NL}})$ of a particular sample at different (z_l, v_l) layers. Different graph cuts (such as blue profiles in Fig. 1) can be considered, where the interaction of each cut with the nodes can be seen as a *nominated* solution of the optimization (9) for all M samples. The energy of each cut can be estimated using the sum of the data term in the interacted nodes and velocity variation in neighborhood samples along the considered cut. Hence, among all possible graph cuts, the solution of (9) is obtained by seeking the graph cut whose energy (sum of the data term and velocity variation) is the minimum between all other possible cuts. Consequently, the unknown parameter ($\hat{\mathbf{z}}$ and $\hat{\mathbf{v}}$) of the M selected samples can be discerned from the intersection of the optimal cut (red profile in Fig. 1) with the nodes. Once, $\hat{\mathbf{z}}$ and $\hat{\mathbf{v}}$ are estimated, the parameters of the pixel of interest, i.e., central pixel p, can be reconstructed. The window moves over the image to repeat this procedure for any other interested cell and compute its unknown parameters. Moreover, it should be noted that the parameter α in (9) indicates the relative importance of the two employed terms. Finally, the reconstruction algorithm can be summarized as:

III. Experimental Results

In this section, the experimental results of the proposed method using the simulated and two real data sets are reported. For the sake of comparison, the proposed regularized ML (9) is compared with the conventional ML process in (7). To implement the regularized ML, a moving window (19×19) around the pixel of interest is considered. Moreover, it is being understood that when α in (9) is zero, the regularized optimization boils down to the conventional

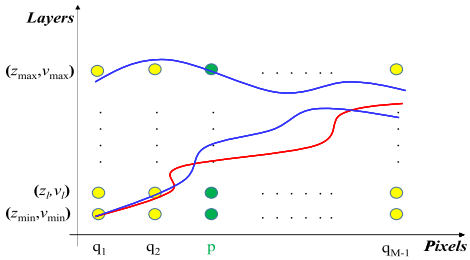

Fig. 1. Graph-cut-based minimization. The red profile has the minimum sum of data term and velocity variation between all possible graph cuts indicated with blue profiles. Green and yellow nodes are related to the center and neighborhood samples, respectively.

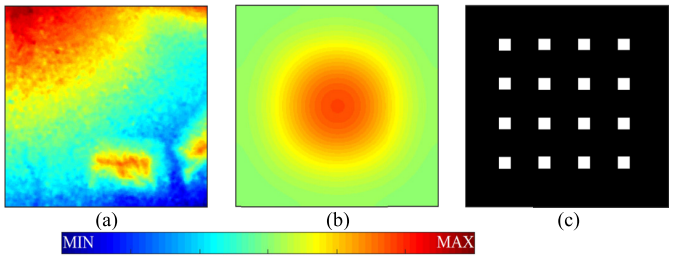

Fig. 2. Simulated data. (a) Simulated terrain height model [0–20] m, (b) true simulated velocity of the scene [−3, 3] cm/year, and (c) mask image.

ML minimization in (7), while its higher values may lead to the oversmoothing effect. In this letter, α is tuned by trial and error and by assessing the results of estimated velocity and residual height maps in different homogeneous and heterogeneous regions. Particularly, the considered criterion for the tuning process is addressing the outliers and artifacts as much as possible while avoiding oversmoothing effects. Moreover, it should be noted that the optimal value of the α parameter can vary with respect to the study area, noise levels, and number of neighborhood samples in the considered window.

A. Simulated Data

The Monte Carlo simulations were proceeded in order to simulate a stack of 19 images (with a size of 512×512), where the spatial and temporal baselines and the system parameters are set to the typical values of the Constellation of Small Satellites for Mediterranean basin Observation (COSMO-SkyMed) data set that is introduced in Section III-B (see Table I). The data were simulated in a favorable scenario over the given terrain height model and the true imposed velocity map in Fig. 2. In order to evaluate the efficiency of the proposed method, the simulated data are corrupted with some artifacts, i.e., temporal decorrelation and atmospheric noise effects in the highlighted white patches in the mask image shown in Fig. 2(c). To impair the data by temporal decorrelation, the coherences are affected by the well-known decorrelation model as $\gamma_{kl} = \gamma_{kl}\ \exp(|t_l - t_k|/\tau)$, where τ is the decorrelation rate, while the atmospheric phase noise is simulated with the zero mean and standard deviation of $\sigma\pi$ from baseline to baseline. The decorrelation rate is set to the particular $\beta\%$ of the total temporal baseline (T), i.e., $\tau = \beta$T. To the aim of extensive analyses, the corruptions were proceeded by variation in both parameters in the range of $\beta \in$ [0.9 0.8 0.7 0.6] and $\sigma \in$ [0.1 0.15 0.175 0.2]. For each pair of (β, σ), both the conventional and regularized MLs were implemented. The first row of Fig. 3 shows the results from the case of $\beta = 0.9$ and $\sigma = 0.1$, while the second row is related to most critical simulated scenario,

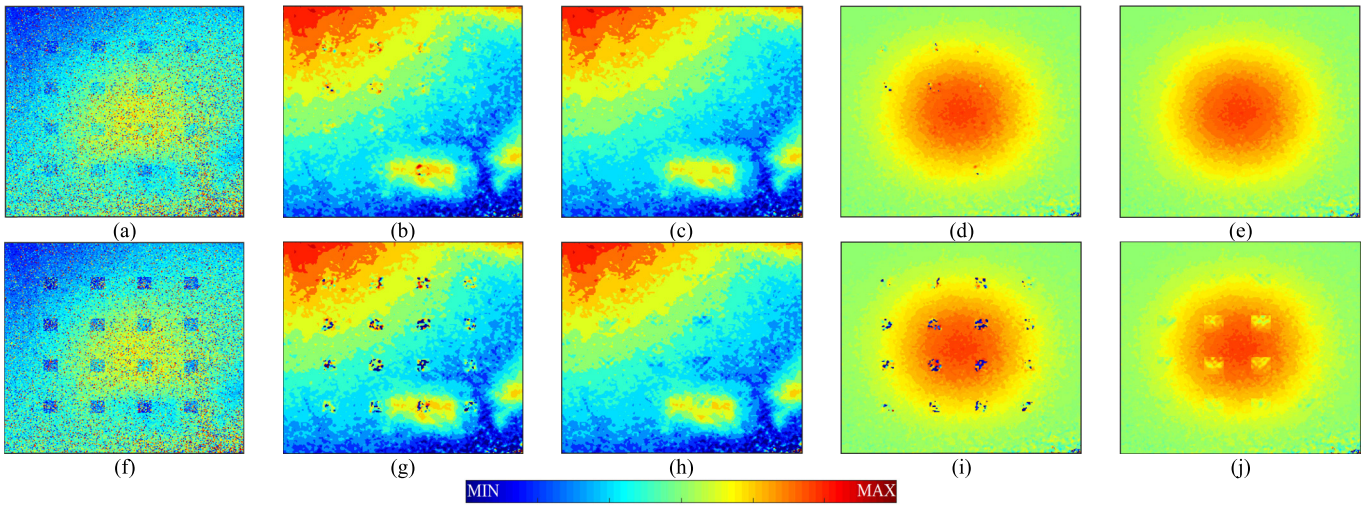

Fig. 3. Estimated interferometric parameters form the corrupted data. The figures in the first row are related to the corrupted data with ($\beta = 0.9$, $\sigma = 0.1$), while the second row is related to the pair of ($\beta = 0.6$, $\sigma = 0.2$). (a) and (f) Corrupted noisy interferograms $[-\pi\, \pi]$. (b) and (g) Estimated elevation [0 20] using the ML approach and (c) and (h) proposed method. (d) and (i) Estimated mean deformation velocity [−3 3] cm/year using the ML approach and (e) and (j) proposed method.

TABLE I

BASELINE DISTRIBUTION OF THE CSK DATA SETS

Spatial baseline **b** (meter)	0	-35.3	300.8	-148.3	439.8	-61.4	-201.3	457.7	374.5	-309.8,	20.4	-77.8	-110.6	324.4	72.5	259.71	110.1	179.9	37
Temporal baseline **t** (day)	0	236	-161	-212	-304	112	-33	-177	32	80	-40	-312	76	-145	-36	128	104	72	-24

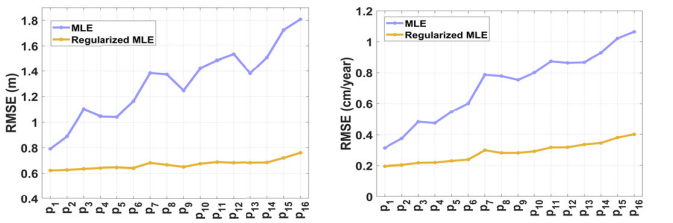

	p_1	p_2	p_3	p_4	p_5	p_6	p_7	p_8	p_9	p_{10}	p_{11}	p_{12}	p_{13}	p_{14}	p_{15}	p_{16}
β	0.9	0.8	0.7	0.6	0.9	0.8	0.7	0.6	0.9	0.8	0.7	0.6	0.9	0.8	0.7	0.6
σ	0.1	0.1	0.1	0.1	0.15	0.15	0.15	0.15	0.175	0.175	0.175	0.175	0.2	0.2	0.2	0.2

Fig. 4. Evaluation of the employed approaches with respect to different temporal decorrelation β and atmospheric σ effects. RMSE of (a) elevation and (b) velocity.

i.e., $\beta = 0.6$ and $\sigma = 0.2$, where both decorrelation and atmospheric effects were increased. For each pair of (β, σ), the root-mean-square error (RMSE) between the estimated and true values of the elevation and velocity maps is computed and plotted in Fig. 4. As can be seen from Figs. 3 and 4, the results by the conventional ML are affected by the imposed artifacts. The spots due to high phase jumps and discontinuities on the results of ML in Fig. 3(b), (d), (g), and (i) affirm that the conventional ML failed to properly estimate the parameters. However, from the visual inspection of the results obtained by the proposed method in Fig. 3(c), (e), (h), and (j), it is apparent that the good performances are achieved by the use of regularization, confirming the robustness of the proposed method to the artifact patches, characterized by high phase jumps and discontinuities. The visual analysis is confirmed by the quantitative evaluation present in Fig. 4 for all possible pairs of β and σ. The RMSE for both elevation and velocity affirms the performance of the proposed method.

B. Real Data Set: COSMO-SkyMed

The first real data were acquired by COSMO-SkyMed (CSK) sensor over the Tehran metropolitan, and it consists of 19 images in X-band acquired between June 2012 and January 2014 with the system operating in the strip-map mode and HH polarization. The image resolution is 1.47 m × 3 m in slant range and azimuth directions, and the baseline information is provided in Table I. A subset of the image (1000 × 600 pixels) was processed using both the employed approaches and the related results are presented in Fig. 5. Note that the processing is limited to the stable scatterers whose ensemble coherence is above the specified threshold (see [1]). However, we refer the readers to [2] for more effective scatterer detection framework based on false alarm probability. In analogy to the simulated experiments, the artifact effects are evident in the results of the conventional ML method [Fig. 5(a) and (c)]. This can be noticed by unexpected variation in the target parameters from pixel to pixel. However, moving to the results by the proposed method [Fig. 5(b) and (d)], the outliers are significantly suppressed by the employment of information from neighborhood samples. The improvements are obtained in both urban (the zoomed area) and nonurban terrain regions (the middle part of the image).

C. Real Data Set: Sentinel-1A

Further investigation on the proposed method was carried out by the experiments using a stack of 15 C-band Sentinel-1A SAR images in VV polarization over the north-west of Tehran, Iran. The spatial (slant range-azimuth) resolution is 5 m × 20 m and subsequently, to utilize a (partially) square window in meters, a rectangular window 19 × 7 was employed within the regularization framework. The test site is a subset of image (1150 × 355 pixels) and includes the Chitgar lake, forest park, and urban area. The images were acquired from February 18, 2017 to January 15, 2019 (See Table II). Moreover, for the considered site, the measurements of a GPS station (see the box in Fig. 6) are available and used to validate the methods. The mean deformation velocity of the station (−3.6 cm/year) is computed from GPS measurements and based on the weighted parametric least square approach [see

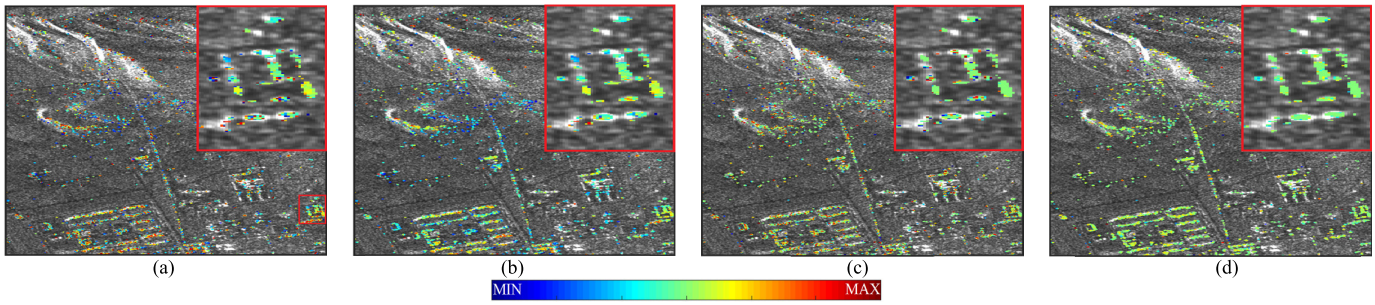

Fig. 5. Experimental results from the CSK data sets. The red box is zoomed in the upper right of the images. (a) and (b) Residual height [−40 40] m and (c) and (d) mean velocity [−2.5 2.5] cm/year using the ML and regularized ML. (a) ML. (b) Regularized ML. (c) ML. (d) Regularized ML.

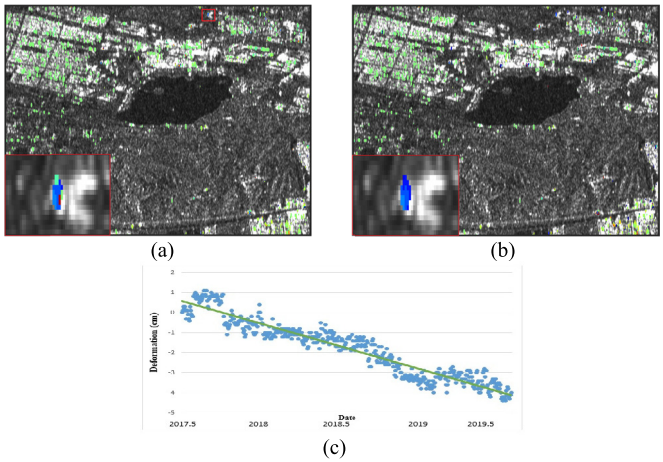

Fig. 6. Mean deformation velocity [−2.5 2.5] cm/year using the Sentinel-1A data sets. The red box is related to the GPS station and zoomed in lower left of the images. (a) ML. (b) Regularized ML. (c) Linear trend of deformation using GPS observations ($d = -3.6t + 0.59$).

TABLE II
BASELINES DISTRIBUTION OF THE SENTINEL-1A DATA SETS

b(m)	0	-60	-17	36	-33	5	55	-23	-57	-18	49	-73	-24	14	-38
t(day)	0	408	360	300	228	180	132	84	36	-24	-72	-120	-168	-216	-288

Fig. 6(c)]. For the sake of conciseness, only the estimated velocity maps are reported in Fig. 6. The candidate pixels inside the red box are around the GPS station (see the zoomed area in the image) and RMSE of their estimated velocity regarding the GPS measurement is 1.31 and 0.35 cm/year for ML and regularized method, respectively. This is in agreement with the qualitative comparison of the reported results in the zoomed area, which confirms the performance of the proposed method.

IV. CONCLUSION

In this letter, a new framework for the estimation of target parameters (the residual height and mean deformation velocity) using MB interferometric data sets was introduced. The proposed method adapts a regularization of the velocity variation over neighborhood pixels into the ML model. The derived nonconvex optimization was resolved using the graph-cut strategy. The proposed method was evaluated on the simulated and two real data sets and compared to the conventional ML. The quantitative and qualitative analyses were carried out to validate the effectiveness of the proposed method, particularly the comparison and validation using GPS-based measurements revealed the efficiency of the proposed technique. The proposed procedure is robust to the outliers and artifacts. Particularly, the method employs the information of neighborhood pixels to provide a reliable solution for the pixel of interest (central pixel), which is impaired by disturbing factors. Note that the improvement by the regularization is paid at the cost of computational efforts. Finally, it should be noted that the proposed method might be limited by the suppression of true local variations of velocity in urban areas. This possible issue can be addressed by setting a relatively lower importance to the regularization term (i.e., velocity variation) in the heterogeneous regions, such that the solution of the proposed method approaches to the result by the conventional ML. Hence, the benefits of adaptive estimation of α parameter based on the homogeneity/heterogeneity information should be assessed.

ACKNOWLEDGMENT

The authors would like to thank the anonymous reviewers for their valuable comments, which have improved the quality of this letter and the Italian Space Agency for providing CSK data.

REFERENCES

[1] A. Ferretti, A. Fumagalli, F. Novali, C. Prati, F. Rocca, and A. Rucci, "A new algorithm for processing interferometric data-stacks: SqueeSAR," *IEEE Trans. Geosci. Remote Sens.*, vol. 49, no. 9, pp. 3460–3470, Sep. 2011.

[2] A. Pauciullo, D. Reale, W. Franze, and G. Fornaro, "Multi-look in GLRT-based detection of single and double persistent scatterers," *IEEE Trans. Geosci. Remote Sens.*, vol. 56, no. 9, pp. 5125–5137, Sep. 2018.

[3] F. Baselice, A. Budillon, G. Ferraioli, V. Pascazio, and G. Schirinzi, "Multibaseline SAR interferometry from complex data," *IEEE J. Sel. Topics Appl. Earth Observ. Remote Sens.*, vol. 7, no. 7, pp. 2911–2918, Jul. 2014.

[4] G. Ferraioli, C.-A. Deledalle, L. Denis, and F. Tupin, "Parisar: Patch-based estimation and regularized inversion for multibaseline SAR interferometry," *IEEE Trans. Geosci. Remote Sens.*, vol. 56, no. 3, pp. 1626–1636, Mar. 2018.

[5] Y. Wang and X. X. Zhu, "Robust estimators for multipass SAR interferometry," *IEEE Trans. Geosci. Remote Sens.*, vol. 54, no. 2, pp. 968–980, Feb. 2016.

[6] H. Ishikawa, "Exact optimization for Markov random fields with convex priors," *IEEE Trans. Pattern Anal. Mach. Intell.*, vol. 25, no. 10, pp. 1333–1336, Oct. 2003, doi: 10.1109/TPAMI.2003.1233908.

[7] C.-A. Deledalle, L. Denis, F. Tupin, A. Reigber, and M. Jager, "NL-SAR: A unified nonlocal framework for resolution-preserving (Pol)(In)SAR denoising," *IEEE Trans. Geosci. Remote Sens.*, vol. 53, no. 4, pp. 2021–2038, Apr. 2015.

[8] J. W. Goodman, "Some fundamental properties of speckle," *J. Opt. Soc. Amer.*, vol. 66, no. 11, pp. 1145–1150, Nov. 1976.

[9] G. Fornaro, D. Reale, and F. Serafino, "Four-dimensional SAR imaging for height estimation and monitoring of single and double scatterers," *IEEE Trans. Geosci. Remote Sens.*, vol. 47, no. 1, pp. 224–237, Jan. 2009.

[10] H. Aghababaee, G. Ferraioli, G. Schirinzi, and V. Pascazio, "Regularization of SAR tomography for 3-D height reconstruction in urban areas," *IEEE J. Sel. Topics Appl. Earth Observ. Remote Sens.*, vol. 12, no. 2, pp. 648–659, Feb. 2019.